Article

Synthesis and Characterization of CuZnSe Nanocrystals in Wurtzite, Zinc Blende and Core-Shell Polytypes

Huan Ren, Miao Wang, Zhe Li, Fathima Laffir, Grace Brennan, Yuanwei Sun, Killian Stokes, Hugh Geaney, Emmet J. O'Reilly, Peng Gao, Ning Liu, Conor McCarthy, and Kevin M. Ryan

Chem. Mater., **Just Accepted Manuscript** • DOI: 10.1021/acs.chemmater.9b03063 • Publication Date (Web): 25 Nov 2019

Synthesis and Characterization of $CuZnSe_2$ Nanocrystals in Wurtzite, Zinc Blende and Core-Shell Polytypes

Huan Ren[#†], Miao Wang[#‡], Zhe Li[†], Fathima Laffir[†], Grace Brennan[†], Yuanwei Sun[§], Killian Stokes[†], Hugh Geaney[†], Emmet J. O'Reilly[†], Peng Gao[§], Ning Liu[†], Conor McCarthy[†], Kevin M. Ryan[*†]

[†] Department of Chemical Sciences and Bernal Institute, University of Limerick, Ireland
‡Suzhou Institute of Nano-tech and Nano-bionics, Chinese Academy of Sciences, Suzhou, P.R.China
[§]International Center for Quantum Materials and Electron Microscopy Laboratory, School of Physics, Peking University, Beijing, P.R.China
*Corresponding author
[#]These authors have made equal contributions

Abstract- $CuZnSe_2$ (CZSe) is an important ternary semiconductor comprised of earth-abundant elements with a suitable bandgap for visible light absorption and structural/stoichiometric versatility that make it a promising candidate for photovoltaic applications. Here we report the controlled synthesis of this compound copper chalcogenide in nanocrystal form using a colloidal hot-injection approach. Furthermore, we demonstrate control over the crystal phase to occur either as wurtzite (WZ) or zinc blende (ZB) as a function of the presence and absence of phosphorous-based ligands. A major emission peak was observed at ~1.7 eV using low-temperature photoluminescence (PL), ranging from 30 K to 200 K. Additionally, we demonstrate the ability to extend this synthetic protocol to form a polytype structure comprised of a ZB core with a WZ shell.

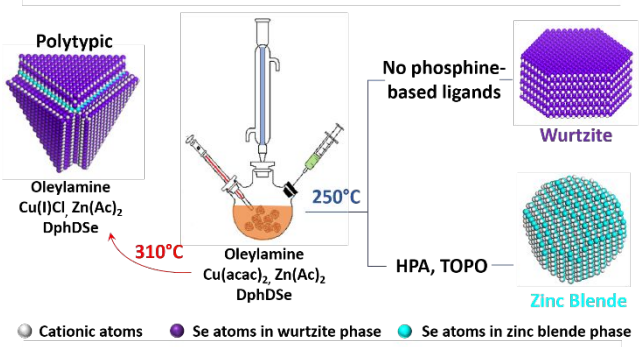

I. Introduction

Copper-based multicomponent colloidal nanocrystals (NCs) are an important category of colloidal NCs due to their high light absorption coefficients, band gap energy tunability, relatively low-toxicity and high earth-abundance.[1] Amongst many common bottom-up synthesis protocols, colloidal hot injection syntheses have proven to be a versatile approach to generate a wide range of compound copper chalcogenide NCs comprised of multiple additional metal cations from main group (e.g. Sn) and transition metal sources (e.g. Fe). These cation substitutions in ternary and quaternary copper chalcogenide systems, along with the morphology modification possible due to the range of crystal phases allow for particle design by composition, size and structure. In addition, the occurrence and control of polytypism in these copper chalcogenides have allowed for even greater complexity in shape as a function of nucleating in one phase with a switch to growth in the alternate.[2-5] The ability to control composition, as a function of the ratio of elements, allows for a facile band gap tuning that is not size dependent to the small Bohr radius of these materials (typically ~2.5 nm).[1, 6-8]

From a functional application perspective, ternary and quaternary copper-based chalcogenides with indirect bandgap structures, designed for non-radiative applications can be conceptually derived from II-VI (e.g. CdTe) binary chalcogenides with direct bandgaps by complete replacement of the divalent cations (e.g. Zn[9-12], Fe[13-15], Cd[4, 5]) by monovalent cations (e.g. Cu) and other cations of various valence (III- Al[16-18], Ga[19-21], In[22-29]; IV-Sn[3, 30-32], Ge[33-35]; V- Sb[36-38], Bi[39, 40]). A number of groups have used this ability to tune composition in addition to nanoscale morphology to attain desired physical and chemical properties.[1, 41, 42] In the well-studied I-III-VI systems, the composition can be tuned in a broad range, both stoichiometrically and non-stoichiometrically due to the ability to exploit defects or vacancies of the I and III species.[43] We previously reported a complete study on the modulating effect of NC shape control and crystal phase for ternary Cu_2SnSe_3 (I_2-IV-VI_3), with the bandgap energy changing from 1.34 to 1.54 eV[31]. There are some interesting observations from related ternary composition in thin films where, for example, a variation of the Cu to Cd ratio makes a $Cu_{1-x}Cd_xS_2$ thin film change its conductivity type between p-type and n-type.[44] A similar conclusion was reached for CuZnS sprayed films, where conductivity changes of 4

orders of magnitude, as a function of the Cu concentration were reported.[45] In a further derivation of this structure with Zn addition to form the quaternary (I-II-IV-VI system ($Cu_2ZnSn(S_xSe_{1-x})_4$), chemical composition ratio tuning and crystal structure control allowed tuning of the bandgap from 1.4 eV to 0.9 eV.[46] The emission behavior of Cu_2ZnSnS_4 polycrystals at 10 K was further studied where two PL emission bands at 1.27 and 1.35 eV were induced by band-to-impurity recombination due to the deep defect states.[47]

While a broad range of compositions in ternary and quaternary chalcogenides have been formed, there are combinations that have remained elusive. In particular, $CuZnSe_2$ has not been directly formed and is interesting as it only consists of earth-abundant elements and has significant potential in solar cells, catalysis and thermoelectrics. Zn inclusion to date has only been achievable in the quaternary form, with a ternary intermediate. For example $CuZnInSe_3$[48] derived from Cu_2InSe_3 or $Cu_2ZnSnSe_4$[49-51] derived from Cu_2SnSe_3. Although there has been some success with cation exchange of Cu in binary Zn sulphide/selenide NCs[52-54] to make ZnSe:Cu/ZnS:Cu NCs, it is attractive to tune the electronic and/or optical properties via direct Zn and Cu incorporation.

Herein, we report a direct colloidal hot injection synthesis of $CuZnSe_2$ NCs with a tight size distribution. Furthermore, we demonstrate crystal phase control using phosphorus-based ligands while the reaction temperature, precursors and solvent remain unvaried. The presence of phosphorus-based ligands completely favored ZB crystals whereas their absence favored WZ. Moreover, polytypic CZSe NCs were successfully synthesized with a zinc-blende core and wurtzite shell. The particles are characterized by HRTEM, electron diffraction, EDX, XRD, and Raman and temperature-dependent photoluminescence combined with atomic modelling

II. CHEMICALS AND EXPERIMENTAL PROCEDURE

Materials. copper(II) acetylacetonate ($Cu(II)(acac)_2$; Sigma Aldrich, >99.99 %), copper(I) chloride (Cu(I)Cl; Sigma Aldrich, >99.99 %), zinc acetate ($Zn(Ac)_2$, Sigma Aldrich, >99.99 %), hexylphosphonic acid (HPA, Sigma Aldrich, >95 %), triotylphosphic oxide (TOPO, Sigma Aldrich, >99%), diphenyl diselenide (DPDSe, Sigma Aldrich, 98 %), oleylamine (OLAM, Sigma Aldrich, technical grade, 70 %) were purchased from Sigma Aldrich. All chemicals were used as purchased without further processing.

Synthesis of WZ CZSe NCs (Hexagonal Plates). In a typical synthesis, $Cu(II)(acac)_2$ (0.5 mmol), and OLAM (10 ml) were added in a three-neck flask and evacuated at 60 °C for 20 min. The solution was then heated to 250 °C in 15 min under the protection of argon. Injection solution 1 consisted of DPDSe (0.625 mmol) and OLAM (2.5 ml), injection solution 2 consists of $Zn(Ac)_2$ (0.25 mmol) and OLAM (1.5 ml). Injection solution 1 was injected to the mother solution in a three-neck flask at 155°C via a syringe, injection solution 2 was injected 20 seconds after the first injection. After the mother solution temperature reached 250 ˚C, the reaction was allowed to proceed at this temperature for another 10 minutes with continuous stirring from a magnetic stirrer. The reaction was terminated by removing the heating mantle and quenched with 30 ml of toluene when the temperature was cooled to 90 °C naturally.

Synthesis of ZB CZSe NCs (Spherical Particles). In a typical synthesis, $Cu(II)(acac)_2$ (0.5 mmol), HPA (0.5 mmol), TOPO (0.5 mmol) and OLAM (8 ml) were added in a three-neck flask and evacuated at 60 °C for 20 min. The solution was then heated to 250 °C in 15 min under the protection of argon. Injection solution 1 consisted of DPDSe (0.3125 mmol) and OLAM (2.5 ml). Injection solution 2 consisted of $Zn(Ac)_2$ (0.25 mmol) and OLAM (1.5 ml). Injection solution 1 was injected into the mother solution in a three-neck flask at 155 °C via a syringe with solution 2 injected 20 seconds later. After the mother solution temperature reached 250 °C, the reaction was allowed to proceed at this temperature for another 10 min with continuous stirring from a magnetic stirrer. The reaction was terminated by removing the heating mantle and quenched with 30 ml of toluene when the temperature was cooled to 90 °C naturally.

Synthesis protocol of Polytypic Structure. In a typical synthesis, Cu(I)Cl (0.25 mmol) and OLAM (10 ml) were added in a three-neck flask and evacuated at 60°C for 20 min. The solution was then heated to 310 °C in 15 min under the protection of argon. Injection solution 1 consisted of DPDSe (0.25 mmol) and OLAM (2.5 ml). Injection solution 2 consisted of $Zn(Ac)_2$ (0.25 mmol) and OLAM (1.5 ml). Injection solution 1 was injected into the mother solution in a three-neck flask at 310 °C via a syringe followed by solution 2 after 7 seconds. After the mother solution temperature reached 310 °C, the reaction was allowed to proceed at this temperature for another 10 min with continuous stirring from a magnetic stirrer. The reaction was terminated by removing the heating mantle and quenched with 30 ml of toluene when the temperature was cooled to 90 °C naturally.

III. RESULTS AND DISCUSSION

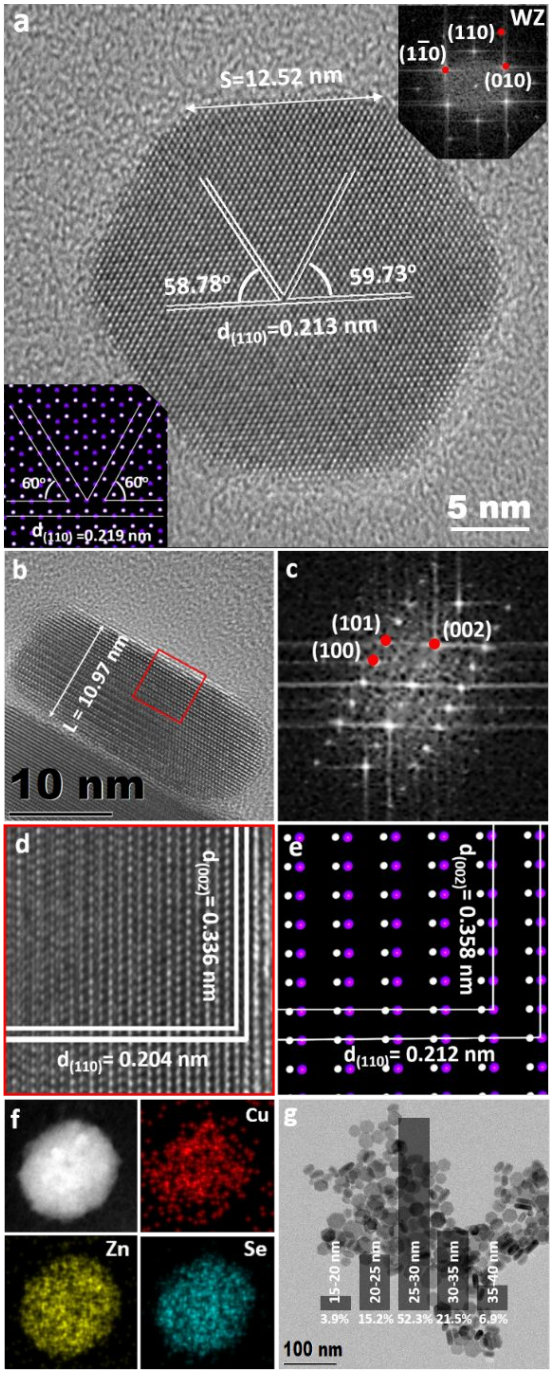

Figure 1. (a) HRTEM image of a single hexagonal WZ $CuZnSe_2$ plate NC from the [0002] direction; corresponding fast Fourier transform (FFT) (top inset); corresponding atomic modelling showing cations white and Se purple (bottom insertion)- (b) HRTEM image of a single hexagonal WZ $CuZnSe_2$ plate nanocrystal with (c) Corresponding FFT, (d) Enlarged lattice fringes from selected area in b. (e) Corresponding atomic modelling of d. (f) STEM image of a hexagonal WZ $CuZnSe_2$ plate NC with corresponding STEM-EDS elemental maps related to Cu (red), Zn (yellow) and Se (cyan). (g) Low magnification TEM image of WZ CZSe NCs with corresponding size distribution histogram.

The synthesis protocol for WZ CZSe NCs involved the use of Cu(II)$(acac)_2$ and diphenyl diselenide in the initial nucleation stage with the Zn precursor ($Zn(Ac)_2$) subsequently introduced via a separate injection. The segregation of the Cu precursor and Zn precursor induced homogeneous nucleation between Cu and Se without the partition of Zn. Figure 1a shows a HRTEM image of a typical WZ CZSe hexagonal nanoplate with a side length of 12.52 nm. The top right inset of the FFT from the WZ [0002] direction is used to calculate *d*-spacings and reveal the crystal phase. The three equivalent (110) facets have a *d*-spacing of ~0.21 nm and form ~60-degree angles with one another, which is in good agreement with the atomic modelling in the bottom left inset. HRTEM in Figure 1b allows further analysis of the WZ crystal structure from a WZ CZSe plate on its edge with a thickness of ~11 nm. The highlighted area in Figure 1b is presented as Figure 1d and demonstrates the ABABA… packing characteristic of the WZ crystal phase viewed along its *c*-axis ([0002] growth direction). The calculated *d*-spacing of the (002) facet from FFT is ~0.39 nm (Figure 1c). The measured *d*-spacing and indexed lattices are also in good agreement with atomic modelling in Figure 1e. STEM-EDS mapping (Figure 1f) confirms the presence and homogeneous distribution of three elements within the nanostructure. Energy dispersive X-ray spectroscopy was used to determine the chemical composition and measurement of three randomly selected areas gave an average composition of Cu:Zn:Se = 1.12:1.00:2.09 (Figure S3a-S3c and Table S1). The WZ CZSe NCs are slightly Cu-rich and Se-poor (Cu/Zn = 1.12; Se/(Cu+Zn) = 0.99), which is consistent with inductively coupled plasma (ICP) analysis (Table S2). The lower magnification TEM image displays the uniformity of WZ CZSe NCs with a relatively narrow size distribution as shown in the corresponding histogram (Figure 1g). More TEM images of WZ NCs can be found in Figure S1.

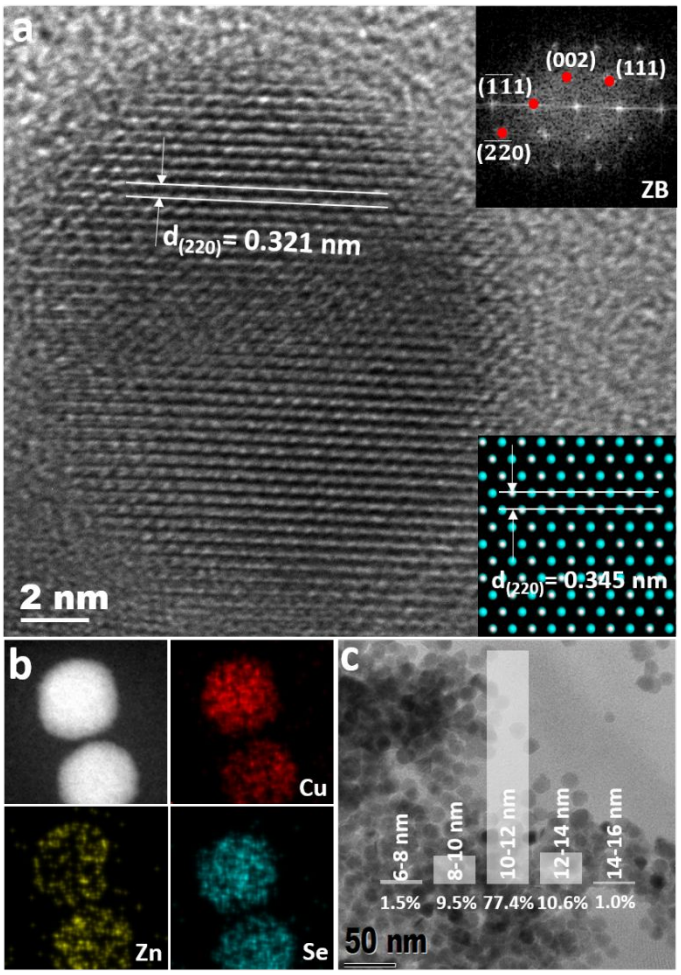

Figure 2. (a) HRTEM image of a single spherical ZB $CuZnSe_2$ nanocrystal, with the corresponding fast Fourier transform (FFT) (top inset) and corresponding atomic modelling (bottom inset) with cations white and Se purple; (b) STEM image of spherical ZB CZSe NCs with corresponding STEM-EDS elemental map related to Cu (red), Zn (yellow) and Se (cyan). (c) Low magnification TEM image of ZB CZSe NCs with corresponding size distribution histogram.

The formation of ZB NCs was achieved by inclusion of trioctylphosphine oxide (TOPO) and hexyl phosphonic acid (HPA) into the synthesis protocol. Figure 2a is a HRTEM image of a ZB CZSe nanocrystal that is spherical in shape with a diameter of ~13 nm. The (002) *d*-spacing as calculated from FFT (top inset) is ~0.32 nm. The HRTEM image of the ZB NC is slightly off-angle to the most-exposed ZB (111) facet which is confirmed by the slight difference between modelled and directly measured *d*-spacings (~0.35 nm versus ~0.32 nm). The STEM-EDS elemental mapping (Figure 2b) confirms the presence and homogeneous distribution of Cu (red), Zn (yellow) and Se (cyan) within the NCs. The low magnification TEM image with the corresponding size distribution histogram presented in Figure 2c shows the uniformity of ZB CZSe NCs achieved using this synthetic approach. More TEM images are included in Figure S2. Again, energy dispersive X-ray spectroscopy was used to measure the chemical composition where an average composition of Cu:Zn:Se = 1.00:1.08:2.02 (Figure S3d-S3f and Table S1) was observed following the measurement of three randomly selected areas. The ZB CZSe NCs are slightly Zn-rich and selenium-poor (Cu/Zn = 0.93; Se/(Cu+Zn) = 0.97), in good agreement with ICP analysis (Table S2).

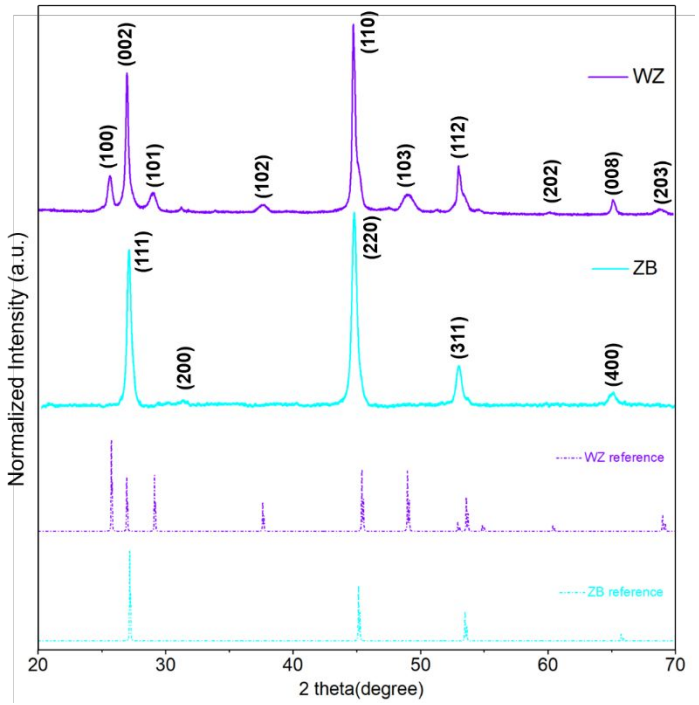

Figure 3. XRD pattern of WZ $CuZnSe_2$ NCs and ZB $CuZnSe_2$NCs with simulated WZ and ZB XRD patterns.

The structure of the as-synthesized NCs was characterized by X-ray diffraction (XRD), as shown in Figure 3. The main reflections for WZ are at 25.6°, 26.9 °, 29.0°, 37.7°, 44.8°, 48.9°, 53.1°, 60.3°, 65.3°, 68.9° and can be respectively indexed to the (100), (002), (101), (102), (110), (103), (112), (202), (008) and (203) planes of the wurtzite structure. Five reflections at 27.2°, 31.6°, 45.1°, 53.4°, 65.6° can be indexed to (111), (200), (220), (311) and (400) planes of zinc blende structure, respectively. The lattice parameters were calculated from the experimental XRD pattern by fitting the main diffraction peaks corresponding to the cubic and wurtzite structures. The lattice parameters of WZ are a = b = 4.0192 Å and c = 6.7112 Å calculated from the fitting of (002) and (110) planes. The lattice parameter calculated for the cubic structure is a = 5.7910 Å, calculated from the fitting of the (111) plane. The completed peak lists and corresponding plane indexes can be found in Table S3 and

Table S4. These calculated lattice parameters along with the crystal structures were derived from ZnSe, by randomly substituting partial Zn ions with Cu ions.

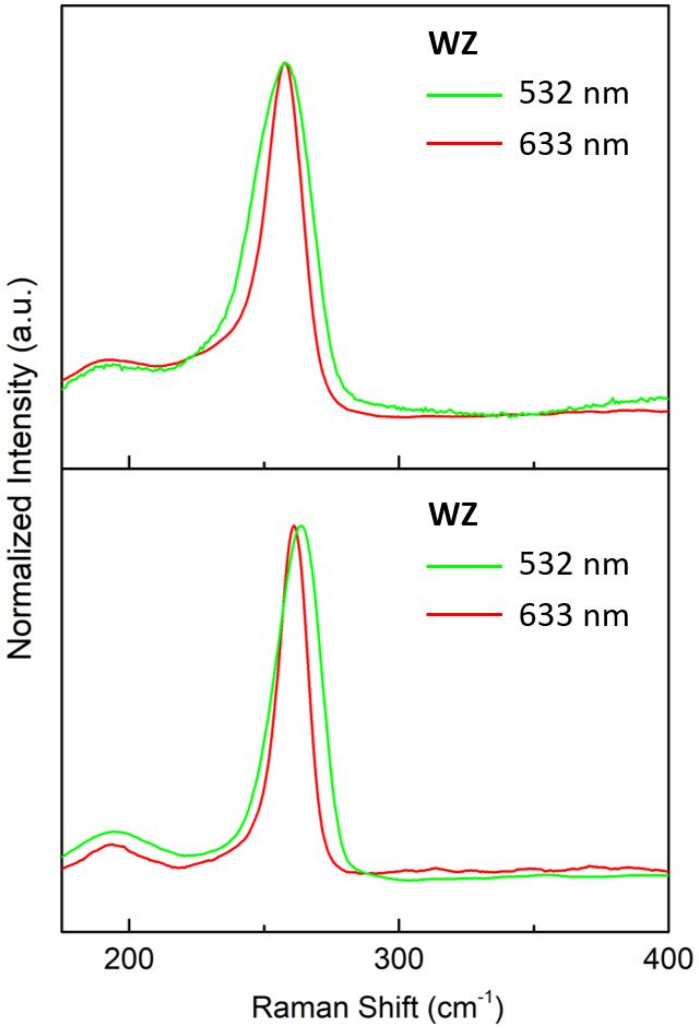

Figure 4. Raman spectra of WZ CZSe NC sample and ZB CZSe NC sample excited under 532 nm green laser and 632.8 nm red laser respectively.

Raman spectra of the NCs under two excitation lasers (532 nm and 632.8 nm) are shown in Figure 4. Both the WZ and ZB spectra have a major peak at ~260 cm^{-1} and one less intense peak at ~193 cm^{-1}. In previous research, for Cu_3Se_2 and Cu_2Se reference spectra[55, 56], the major peak occurs at ~260 cm^{-1}, with a less intense peak at ~190 cm^{-1}. ZnSe reference spectra[57-59]have been reported with two major peaks at ~200 cm^{-1} (the less intense longitudinal optical phonon mode, LO $^{-1}$) and ~260 cm^{-1} (the transverse optical phonon mode (TO). Therefore, the most intense peak at 260 cm^{-1} observed in our CZSe spectra can be attributed to the overlapping of Cu_3Se_2/Cu_2Se and ZnSe peaks with the less intense peak at ~193 cm^{-1}arising from the LO modes of Cu_3Se_2/Cu_2Se and ZnSe.

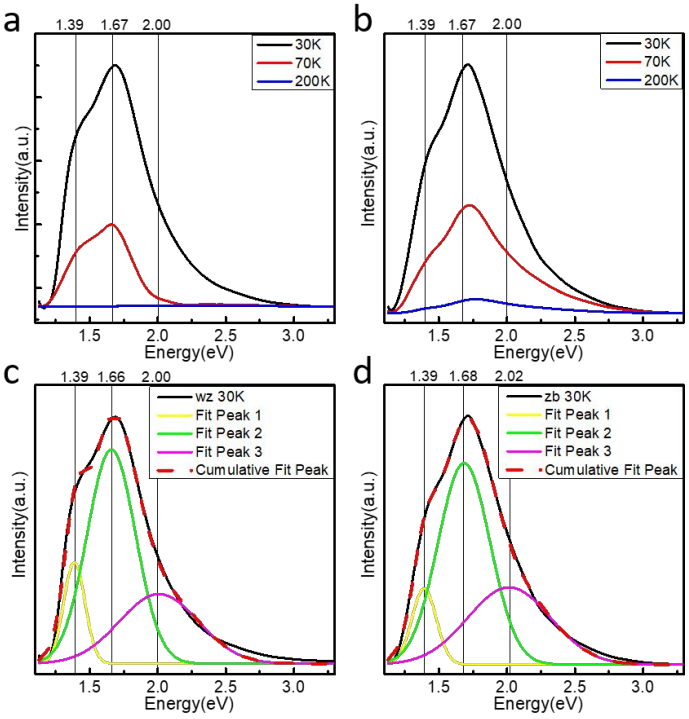

Figure 5. Temperature-dependence photoluminescence spectra of (a) WZ NC sample and (b) ZB NC sample; Low-temperature photoluminescence spectra (30 K) Gaussian fitting of (c) WZ NC sample and (d) ZB NC sample.

To further investigate the optical properties of the CZSe NCs, temperature-dependent photoluminescence (PL) tests were carried out at an excitation wavelength of 325 nm and laser power of ~5 mW (Figure 5). Both WZ and ZB CZSe NCs show low quantum efficiency at room temperature, suggesting that these CZSe NCs have indirect bandgap structures or crystal phase defects. No emission peaks were observed for the WZ CZSe NCs at 200 K, while for ZB CZSe NCs a weak signal peak was observed (Figure 5a-b). When the temperature was decreased to 70 K, the PL intensity of both materials was observed to increase significantly. At 30 K, the PL intensity increased a further threefold for both NCs. This broad peak was determined through Gaussian peak fitting (Figure 5c, 5d) to arise from separate peaks at ~1.39 eV, ~1.67 eV, and ~2.00 eV where their positions and relative intensities remained constant at varying temperature. These peaks are likely due to indirect band hybridization. When compared to relevant binary systems (CuSe at ~2.2 eV[60, 61] ; ZnSe at ~2.3 eV and ~3.2 eV[62-64]), the incorporation of Cu in the ZnSe structure causes a downshift of emission energy. Furthermore, the different electronic configurations of the two cations complicates the hybridized $CuZnSe_2$ band structure, likely giving rise to the low PL emission intensities at room temperature.

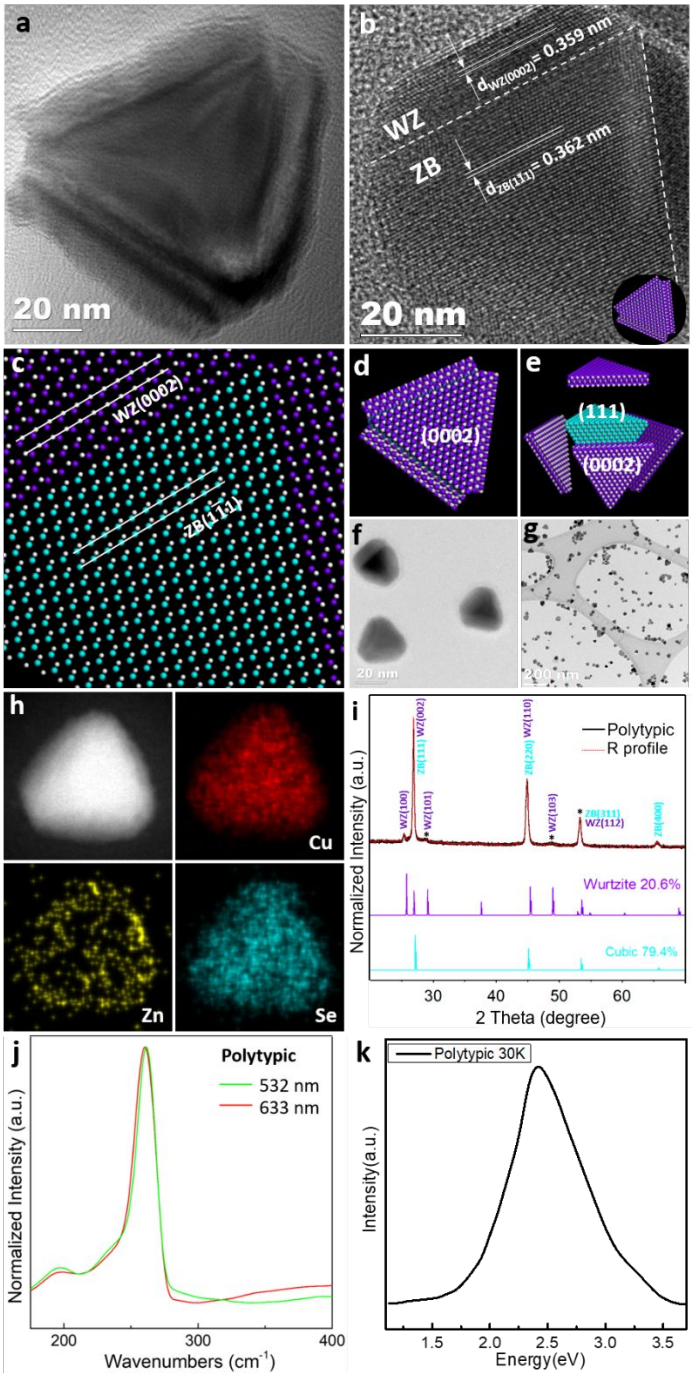

Figure 6. (a) TEM image of a CZSe polytypic NC. (b) TEM image of a CZSe polytypic NC from ZB[011] direction showing the polytypic interphase between the ZB and WZ phases (bottom inset is corresponding structural model) (c) Scaled-up structural model of b to show atomic positions (d) Corresponding atomic structural modelling of a. (e) Cut away atomic structural modelling of a CZSe polytypic NC. (f) TEM image of three CZSe polytypic NCs. (g) Low magnification TEM of CZSe polytypic NCs. (h) STEM image of a polytypic CZSe NC with corresponding STEM-EDS elemental maps related to Cu (red), Zn (yellow) and Se (cyan). (i) XRD pattern of CZSe polytypic NCs with ZB and WZ phases XRD reference patterns, along with the Rietveld Refinement peak fitting reflecting the ZB and WZ phase ratio. (j) Raman spectrum of CZSe polytypic sample under 632.8 nm (red) and 532 nm (green) respectively. (k) Low-temperature photoluminescence spectrum of CZSe polytypic sample (30 K) with Gaussian fitting.

A tetrahedral-shaped polytypic structure (~ 40 nm in diameter), with ZB core and four thin outer WZ triangular plates was formed in the absence of phosphorus-based ligands when the nucleation precursor was changed from $Cu(acac)_2$ to Cu(I)Cl at a raised temperature of 310 °C (Figure 6a). The contrast difference within the structure highlights the tetrahedral core, where clear polytypic interfaces are observed in conjunction with a flat outer crystal. The ZB core here is a perfect tetrahedron as opposed to a quasi-sphere ZB core previously reported for tetrapod NCs[3, 65-67]. A further difference here is the preference for the WZ to form into short ~ 5 nm triangular platelets rather than relatively high aspect ratio rod elongation. As shown in Figure 6b, when viewed from the ZB[011] direction (shown in bottom right inset), the polytypic interphase separating ZB(1$\bar{1}$1) and WZ(0002) facets can be clearly observed. The *d*-spacing of the WZ(0002) lattice, indexed from the ABABA arrangement along WZ c-axis， is ~0.36 nm whereas the *d*-spacing between the parallel ZB(1$\bar{1}$1) facets is ~0.36 nm. Figure 6c shows the corresponding atomic model of this polytypic structure with further interpretations outlined in Figure 6d and Figure 6e. The interphases of the polytypic structure were determined to be ZB(1$\bar{1}$1) and WZ(0002) arising from initial growth along the ZB[111] direction followed by growth in WZ[0002]. The TEM image in Figure 6f shows three polytypic NCs where the darker contrast reflects the cores. In Figure 6g, the low-magnification TEM image confirms the relatively narrow size distribution (Figure S4) of CZSe polytypic NCs with details on the centrifuge separation process described in supporting information. STEM-EDS mapping (Figure 6h) confirms the presence of three elements within the nanostructure. The high distribution of Zn in the shell area and relatively low distribution in the core area suggests that the core is Zn-poor or potentially binary (Cu_2Se) in composition. Energy dispersive X-ray spectroscopy of three randomly selected areas gave an average composition of Cu:Zn:Se = 2.74:1.00:2.40 (Figure S3g-S3i and Table S1)), which is consistent with ICP results shown in Table S2. The crystallographic composition of the as-synthesized Polytypic structure NCs was confirmed by X-ray diffraction (XRD), as shown in Figure 6i and Table S5 with Rietveld refinement giving WZ and ZB phases at 20.6% and 79.4%, respectively. The Raman spectrum in Figure 6j shows that the polytypic sample has a main peak at (~258 cm^{-1}) and one weak peak at (~192 cm^{-1}), consistent with the single crystal

samples. One new shoulder peak emerges at ~231 cm^{-1} that be assigned to the weak peak of CuSe[68] at ~230 cm^{-1} in agreement with the binary core conclusion. In low-temperature PL analysis (30 K), as shown in Figure 6k, the polytypic structure's main emission peak shifts to a considerably higher energy at ~2.5 eV compared to its pure phase structure (~1.6 eV). The main emission peak is at similar position with the reference peak of Cu_xSe (~2.2 eV)[60, 61], further suggesting the presence of Cu_xSe_y binary phase.

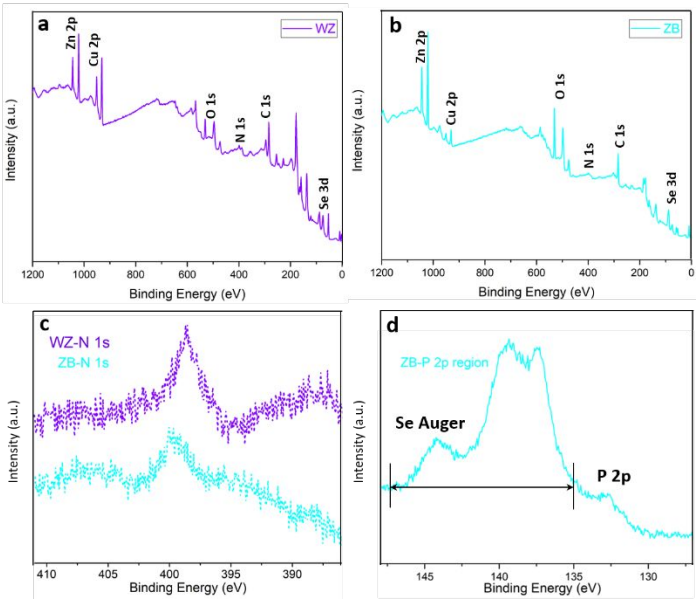

Figure 7. (a) XPS survey of WZ NCs, (b) XPS survey of ZB NCs. (c) high-resolution XPS spectra of N1s in WZ and ZB NCs. (d) high-resolution XPS spectrum of P2p region of ZB NCs.

X-ray photoelectron spectroscopy (XPS) was performed to investigate the surface chemistry of the CZSe NCs. The survey spectra of the as-synthesized NCs show the presence of Cu, Zn, Se, N, O, C (shown in Figure 7a, 7b). The phosphorous region overlaps with the Se LMM Auger peaks. However, the high-resolution spectrum of the P 2p region allows resolution of the peaks and elemental composition in Table S6. For WZ NCs, the XPS quantification shows a Cu/Zn ratio of 0.9, which is consistent with the chemical composition analysis with STEM-EDX and ICP. However, the XPS quantification of ZB NCs (Cu/Zn=0.2) suggests that ZB NCs have a significantly Zn rich and Cu poor surface. High resolution spectra of N 1s (Figure 7c) shows a peak at a binding energy ~400 eV in both WZ and ZB NCs, which corresponds to the N-C bonding of the amine ligands.[69] However, a significant difference is observed in the nitrogen content, with WZ NCs giving a (Zn+Cu)/N ratio of 5.2 and ZB NCs having a ratio of 10.4. This indicates a substantial reduction in the nitrogen-containing OLAM ligands on the ZB NCs surface. High resolution spectra in the P 2p region of the ZB NCs (Figure 7d) shows a phosphate peak at binding energy ~133 eV which can be attributed to the attachment of the HPA/TOPO ligands. It is likely on the ZB NCs surface that the nitrogen-containing OLAM ligand shortage is compensated by the attachment of the phosphorous-containing HPA+TOPO used in the synthesis. The relative concentrations of P and N are 4.6% (atomic) and 1.7% (atomic) respectively, suggesting more phosphorous-based ligands are attached to the surface of ZB NCs than OLAM.

Our previous research has shown that precursor choice based on their decomposition kinetics at selective temperatures is crucial to control of crystal phase formation in the multicomponent copper chalcogenide system[23,24]. Here, in the formation of CZSe, the occurrence of either crystal phase is controlled solely by the addition of phosphorus-based ligands. There is typically a very small energy difference between the growth in WZ and ZB phases (≤20 meV/atom) and a small perturbation can induce a nucleation preference for one or the other[69, 70]. While this perturbation is most often observed as a thermodynamic effect,[2, 4] other factors such as precursor selection[71] and their influence on monomer concentration (supersaturation)[72] are relevant. To explain the effect on the presence and absence of the phosphonic acids on the crystal phase control in this study, it is worth considering how they influence both nucleation and growth. A number of studies have shown that the selective adhesion between phosphorous-based surfactants and facets is critical in forming the nucleation clusters that direct the intrinsic ZB phase growth.[73-75] Furthermore, the combination of phosphorous-based surfactants and low reaction temperature produces monomers gradually by slow thermal decomposition of organometallic precursors. This low monomer concentration favours the isotropic growth of ZB phase.[76-79]

In this research, the crystal phase preference is mainly affected by the different bonding types between ligands and NC facets. HPA and TOPO are X-type bonding ligand and L-type bonding ligands respectively.[80-82] TOPO and HPA are often used in combination, where TOPO acts as a stabilizer by bonding to the extra-cations on the NCs as a Lewis base,[77] whereas HPA exhibiting higher coordinating affinity, is used to attach to selective facets to control the growth rate.[81] Compared to the WZ phase, the ZB phase has more charged facets with high-energy low-index and close atomic packing, such as (100) and (111)[69], which are favored by strongly-bonded phosphorous-based ligands. This is consistent with our observation in XPS where the surface of the ZB NCs is predominately bonded to HPA and TOPO ligands. Furthermore, these facets are energetically homogenized with surfactants to minimize the systematic surface energy, which results in the formation of symmetric spheres[33, 83] The 2D shape of the wurtzite particles is likely a result of the selective crystal growth on the six more

exposed peripheral neutral facets, (100) and (010), instead of elongating along the WZ *c*-axis as the charged ±(0002) facets are covered with OLAM. Interestingly, different from the previous single crystal synthesis strategy, the occurrence of polytypism in CZSe is thermodynamically dominated by a high injection temperature (310 °C). In addition, the use of the coordinating surfactant (OLAM) and diphenyl diselenide (DPDSe) as Se precursor likely also contributes to the formation of polytypes. DPDSe has a known tendency to grow in ZB phase at high temperature in the presence of metal chlorides,[2, 71] favoring the nucleation between Cu(I)Cl and DPDSe at high temperature before the injection. At lower temperature after the injection, DPDSe favours WZ growth regardless of the cation species.[2, 31]

IV. CONCLUSION

In summary, we report the synthesis of CZSe NCs in WZ, ZB and polytypic ZB-WZ forms. XRD, Raman, TEM, EDX, ICP, XPS, atomic models and low-temperature photoluminescence were used to study their structural and optical properties. All three types of NCs have low PL quantum efficiency at room temperature with a significant increase in efficiency at lower temperatures. This to our knowledge is the first successful synthesis of CZSe NCs using a hot injection method where the simple control between the formation of WZ and ZB phases is dictated by the presence or absence of phosphorus-based ligands. The introduction of this direct formation method for CZSe NCs with crystal phase control opens a range of new possibilities in photovoltaic and electronic applications.

SUPPLEMENTARY MATERIAL

See supporting information for experimental details, TEM images, EDS details, XRD details, ICP details, XPS details. The supporting information is available free of charge via the internet at http://pubs.acs.org.

ACKNOWLEDGEMENT

This publication has emanated from research conducted with the financial support of Science Foundation Ireland (SFI) under Grant Number 13/IA/1833, Grant Number 16/IA/4629, Irish Research Council (IRC) under Grant Number IRCLA/2017/285 and the National Natural Science Foundation of China, Grant Number 51672007.

Correspondence Author – Kevin M. Ryan, email address: Kevin.M.Ryan@ul.ie, Tel: + 353 (61) 213167

REFERENCES

1. Coughlan, C.; Ibanez, M.; Dobrozhan, O.; Singh, A.; Cabot, A.; Ryan, K. M., Compound copper chalcogenide nanocrystals. *Chem. Rev.* **2017,** 117, (9), 5865-6109.
2. Singh, S.; Ryan, K. M., Occurrence of Polytypism in Compound Colloidal Metal Chalcogenide Nanocrystals, Opportunities, and Challenges. *J. Phys. Chem. Lett.* **2015,** 6, (16), 3141-3148.
3. Wang, J.; Singh, A.; Liu, P.; Singh, S.; Coughlan, C.; Guo, Y.; Ryan, K. M., Colloidal synthesis of Cu_2SnSe_3 tetrapod nanocrystals. *J. Am. Chem. Soc.* **2013,** 135, (21), 7835-7838.
4. Wu, L.; Fan, F.-J.; Gong, M.; Ge, J.; Yu, S.-H., Selective epitaxial growth of zinc blende-derivative on wurtzite-derivative: the case of polytypic $Cu_2CdSn(S_{1-x}Se_x)_4$ nanocrystals. *Nanoscale* **2014,** 6, (6), 3418-3422.
5. Zamani, R. R.; Ibánez, M.; Luysberg, M.; Garcia-Castello, N.; Houben, L.; Prades, J. D.; Grillo, V.; Dunin-Borkowski, R. E.; Morante, J. R.; Cabot, A., Polarity-driven polytypic branching in Cu-based quaternary chalcogenide nanostructures. *ACS Nano* **2014,** 8, (3), 2290-2301.
6. Knowles, K. E.; Hartstein, K. H.; Kilburn, T. B.; Marchioro, A.; Nelson, H. D.; Whitham, P. J.; Gamelin, D. R., Luminescent colloidal semiconductor nanocrystals containing copper: synthesis, photophysics, and applications. *Chem. Rev.* **2016,** 116, (18), 10820-10851.
7. van Embden, J.; Chesman, A. S. R.; Jasieniak, J. J., The Heat-Up Synthesis of Colloidal Nanocrystals. *Chem. Mater.* **2015,** 27, (7), 2246-2285.
8. Persson, C., Electronic and optical properties of Cu_2ZnSnS_4 and $Cu_2ZnSnSe_4$. *J. Appl. Phys.* **2010,** 107, (5), 053710.
9. Xia, C.; Winckelmans, N.; Prins, P. T.; Bals, S.; Gerritsen, H. C.; de Mello Donegá, C., Near-Infrared-Emitting $CuInS_2$/ZnS Dot-in-Rod Colloidal Heteronanorods by Seeded Growth. *J. Am. Chem. Soc.* **2018,** 140, (17), 5755-5763.

10. Singh, S.; Katiyar, A. K.; Midya, A.; Ghorai, A.; Ray, S. K., Superior heterojunction properties of solution processed copper-zinc-tin-sulphide quantum dots on Si. *Nanotechnology* **2017,** 28, (43), 435704.
11. Xu, J.; Hu, Z.; Zhang, J.; Xiong, W.; Sun, L.; Wan, L.; Zhou, R.; Jiang, Y.; Lee, C.-S., Cu_2ZnSnS_4 and $Cu_2ZnSn(S_{1-x}Se_x)_4$ nanocrystals: room-temperature synthesis and efficient photoelectrochemical water splitting. *J. Mater. Chem. A* **2017,** 5, (48), 25230-25236.
12. Coughlan, C.; Ryan, K. M., Complete study of the composition and shape evolution in the synthesis of Cu_2ZnSnS_4 (CZTS) semiconductor nanocrystals. *CrystEngComm* **2015,** 17, (36), 6914-6922.
13. Gabka, G.; Bujak, P.; Żukrowski, J.; Zabost, D.; Kotwica, K.; Malinowska, K.; Ostrowski, A.; Wielgus, I.; Lisowski, W.; Sobczak, J. W., Non-injection synthesis of monodisperse Cu–Fe–S nanocrystals and their size dependent properties. *Phys. Chem. Chem. Phys.* **2016,** 18, (22), 15091-15101.
14. Gabka, G.; Bujak, P.; Ostrowski, A.; Tomaszewski, W.; Lisowski, W.; Sobczak, J. W.; Pron, A., Cu–Fe–S nanocrystals exhibiting tunable localized surface plasmon resonance in the visible to nir spectral ranges. *Inorg. Chem.* **2016,** 55, (13), 6660-6669.
15. Rouchdi, M.; Salmani, E.; Cherrad, H.; Addou, M.; Ez-zahraoui, H.; Hassanain, N.; Mzerd, A., Spray pyrolysis synthesis of $Cu_xFe_{1-x}S_2$ and their structural, electronic and optical properties: Experimental and first-principles study. *Mater. Sci. Eng. B* **2018,** 227, 100-109.
16. Bhattacharyya, B.; Pandit, T.; Rajasekar, G. P.; Pandey, A., Optical Transparency Enabled by Anomalous Stokes Shift in Visible Light-Emitting $CuAlS_2$-Based Quantum Dots. *J. Phys. Chem. Lett.* **2018,** 9, (15), 4451-4456.
17. Vahidshad, Y.; Irajizad, A.; Ghasemzadeh, R.; Mirkazemi, S.; Masoud, A., Structural and optical characterization of nanocrystalline $CuAlS_2$ chalcopyrite synthesized by polyol method in autoclave. *Int. J. Mod. Phys. B* **2012,** 26, (31), 1250179.
18. Chaki, S.; Mahato, K. S.; Deshpande, M., Characterization by X-Ray Peak Broadening Analysis of Wet Chemical Synthesized $CuAlS_2$ Nanoparticles. *Adv. Sci. Lett.* **2014,** 20, (5-6), 1181-1186.
19. Adhikari, S. D.; Dutta, A.; Prusty, G.; Sahu, P.; Pradhan, N., Symmetry Break and Seeded 2D Anisotropic Growth in Ternary $CuGaS_2$ Nanocrystals. *Chem. Mater.* **2017,** 29, (12), 5384-5393.
20. Geng, X.; Liu, H.; Zhai, L.; Xiong, Z.; Hu, J.; Zou, C.; Dong, Y.; Yang, Y.; Huang, S., Colloidal synthesis of $CuGaS_xSe_{2-x}$ nanoribbons mediated by $Cu_{1.75}(SSe)$ nanocrystals as catalysts. *J. Alloys Compd.* **2014,** 617, 961-967.
21. Regulacio, M. D.; Ye, C.; Lim, S. H.; Zheng, Y.; Xu, Q.-H.; Han, M.-Y., Facile noninjection synthesis and photocatalytic properties of wurtzite-phase $CuGaS_2$ nanocrystals with elongated morphologies. *CrystEngComm* **2013,** 15, (26), 5214-5217.
22. Bao, N.; Qiu, X.; Wang, Y.-H. A.; Zhou, Z.; Lu, X.; Grimes, C. A.; Gupta, A., Facile thermolysis synthesis of $CuInS_2$ nanocrystals with tunable anisotropic shape and structure. *Chem. Comm.* **2011,** 47, (33), 9441-9443.
23. Zhong, H.; Zhou, Y.; Ye, M.; He, Y.; Ye, J.; He, C.; Yang, C.; Li, Y., Controlled synthesis and optical properties of colloidal ternary chalcogenide $CuInS_2$ nanocrystals. *Chem. Mater.* **2008,** 20, (20), 6434-6443.
24. Castro, S. L.; Bailey, S. G.; Raffaelle, R. P.; Banger, K. K.; Hepp, A. F., Synthesis and characterization of colloidal $CuInS_2$ nanoparticles from a molecular single-source precursor. *J. Phys. Chem. B* **2004,** 108, (33), 12429-12435.
25. Feng, G.; Feng, J., Tunable optical properties of ternary non-stoichiometric Cu–In–S nanocrystal emitters. *Micro & Nano Lett.* **2016,** 11, (9), 550-553.
26. Whitham, P. J.; Marchioro, A.; Knowles, K. E.; Kilburn, T. B.; Reid, P. J.; Gamelin, D. R., Single-particle photoluminescence spectra, blinking, and delayed luminescence of colloidal $CuInS_2$ nanocrystals. *J. Phys. Chem. C* **2016,** 120, (30), 17136-17142.
27. Norako, M. E.; Brutchey, R. L., Synthesis of metastable wurtzite $CuInSe_2$ nanocrystals. *Chem. Mater.* **2010,** 22, (5), 1613-1615.
28. Leach, A. D.; Macdonald, J. E., Optoelectronic properties of $CuInS_2$ nanocrystals and their origin. *J. Phys. Chem. Lett.* **2016,** 7, (3), 572-583.
29. Leach, A. D.; Shen, X.; Faust, A.; Cleveland, M. C.; La Croix, A. D.; Banin, U.; Pantelides, S. T.; Macdonald, J. E., Defect luminescence from wurtzite $CuInS_2$ nanocrystals: combined experimental and theoretical analysis. *J. Phys. Chem. C* **2016,** 120, (9), 5207-5212.
30. Ghorpade, U. V.; Suryawanshi, M. P.; Shin, S. W.; Kim, I.; Ahn, S. K.; Yun, J. H.; Jeong, C.; Kolekar, S. S.; Kim, J. H., Colloidal wurtzite Cu_2SnS_3 (CTS) nanocrystals and their applications in solar cells. *Chem. Mater.* **2016,** 28, (10), 3308-3317.
31. Wang, J.-j.; Liu, P.; Seaton, C. C.; Ryan, K. M., Complete colloidal synthesis of Cu_2SnSe_3 nanocrystals with crystal phase and shape control. *J. Am. Chem. Soc.* **2014,** 136, (22), 7954-7960.

32. Norako, M. E.; Greaney, M. J.; Brutchey, R. L., Synthesis and characterization of wurtzite-phase copper tin selenide nanocrystals. *J. Am. Chem. Soc.* **2011,** 134, (1), 23-26.
33. Wang, J.-J.; Ryan, K. M., Colloidal synthesis of Cu_2SnSe_3 nanocrystals with structure induced shape evolution. *CrystEngComm* **2016,** 18, (18), 3161-3169.
34. Wang, J.-J.; Liu, P.; Ryan, K. M., A facile phosphine-free colloidal synthesis of Cu_2SnS_3 and Cu_2ZnSnS_4 nanorods with a controllable aspect ratio. *Chem. Comm.* **2015,** 51, (72), 13810-13813.
35. Regulacio, M. D.; Tee, S. Y.; Lim, S. H.; Zhang, Z.; Han, M.-Y., Selective formation of ternary Cu–Ge–S nanostructures in solution. *CrystEngComm* **2018,** 20, (42), 6803-6810.
36. Liu, Y.; Yang, J.; Gu, E.; Cao, T.; Su, Z.; Jiang, L.; Yan, C.; Hao, X.; Liu, F.; Liu, Y., Colloidal synthesis and characterisation of Cu_3SbSe_3 nanocrystals. *J. Mater. Chem. A* **2014,** 2, (18), 6363-6367.
37. Xu, D.; Shen, S.; Zhang, Y.; Gu, H.; Wang, Q., Selective synthesis of ternary copper–antimony sulfide nanocrystals. *Inorg. Chem.* **2013,** 52, (22), 12958-12962.
38. Liang, Q.; Huang, K.; Ren, X.; Zhang, W.; Xie, R.; Feng, S., Synthesis of Cu–Sb–S nanocrystals: insight into the mechanism of composition and crystal phase selection. *CrystEngComm* **2016,** 18, (20), 3703-3710.
39. Yu, G.; Liu, A.; Jin, H.; Chen, Y.; Yin, D.; Huo, R.; Wang, S.; Wang, J., Urchin-shaped $Bi_2S_3/Cu_2S/Cu_3BiS_3$ composites with enhanced photothermal and CT imaging performance. *J. Phys. Chem. C* **2018,** 122, (7), 3794-3800.
40. Chakraborty, M.; Thangavel, R.; Komninou, P.; Zhou, Z.; Gupta, A., Nanospheres and nanoflowers of copper bismuth sulphide (Cu_3BiS_3): Colloidal synthesis, structural, optical and electrical characterization. *J. Alloys Compd.* **2019,** 776, 142-148.
41. Li, J.; Wang, D.; Li, X.; Zeng, Y.; Zhang, Y., Cation Substitution in Earth-Abundant Kesterite Photovoltaic Materials. *Adv. Sci.* **2018,** 5, (4), 1700744.
42. Adachi, S., *Earth-abundant materials for solar cells: Cu_2-II-IV-VI_4 semiconductors*. John Wiley & Sons: Hoboken, NJ, 2015.
43. Yarema, O.; Yarema, M.; Wood, V., Tuning the Composition of Multicomponent Semiconductor Nanocrystals: The Case of I–III–VI Materials. *Chem. Mater.* **2018,** 30, (5), 1446-1461.
44. Kumar, V. N.; Suryakarthick, R.; Karuppusamy, S.; Gupta, M.; Hayakawa, Y.; Gopalakrishnan, R., Effect of precursor concentration on the properties and tuning of conductivity between p-type and n-type $Cu_{1-x}Cd_XS_2$ thin films deposited by a single step solution process as a novel material for photovoltaic applications. *RSC Adv.* **2015,** 5, (29), 23015-23021.
45. Sreejith, M.; Deepu, D.; Kartha, C. S.; Rajeevkumar, K.; Vijayakumar, K., Tuning the properties of sprayed CuZnS films for fabrication of solar cell. *Appl. Phys. Lett.* **2014,** 105, (20), 202107.
46. Singh, A.; Singh, S.; Levcenko, S.; Unold, T.; Laffir, F.; Ryan, K. M., Compositionally tunable photoluminescence emission in $Cu_2ZnSn(S_{1-x}Se_x)_4$ nanocrystals. *Angew. Chem.* **2013,** 52, (35), 9120-9124.
47. Grossberg, M.; Krustok, J.; Raudoja, J.; Raadik, T., The role of structural properties on deep defect states in Cu_2ZnSnS_4 studied by photoluminescence spectroscopy. *Appl. Phys. Lett.* **2012,** 101, (10), 102102.
48. Guc, M.; Oliva, F.; Kondrotas, R.; Alcobe, X.; Placidi, M.; Pistor, P.; Saucedo, E.; Perez‐Rodriguez, A.; Izquierdo‐Roca, V., CuZnInSe$_3$-based solar cells: Impact of copper concentration on vibrational and structural properties and device performance. *Prog. Photovoltaics: Research and Applications*. **2019,** 27, (8), 716-723.
49. Wang, J.-J.; Hu, J.-S.; Guo, Y.-G.; Wan, L.-J., Wurtzite $Cu_2ZnSnSe_4$ nanocrystals for high-performance organic–inorganic hybrid photodetectors. *NPG Asia Mater.* **2012,** 4, (1), e2.
50. Lin, X.; Kavalakkatt, J.; Kornhuber, K.; Abou-Ras, D.; Schorr, S.; Lux-Steiner, M. C.; Ennaoui, A., Synthesis of $Cu_2Zn_xSn_ySe_{1+x+2y}$ nanocrystals with wurtzite-derived structure. *RSC Adv.* **2012,** 2, (26), 9894-9898.
51. Fan, F. J.; Wang, Y. X.; Liu, X. J.; Wu, L.; Yu, S. H., Large‐Scale Colloidal Synthesis of Non‐Stoichiometric $Cu_2ZnSnSe_4$ Nanocrystals for Thermoelectric Applications. *Adv. Mater.* **2012,** 24, (46), 6158-6163.
52. Jana, S.; Srivastava, B. B.; Acharya, S.; Santra, P. K.; Jana, N. R.; Sarma, D.; Pradhan, N., Prevention of photooxidation in blue–green emitting Cu doped ZnSe nanocrystals. *Chem. Comm.* **2010,** 46, (16), 2853-2855.
53. Hao, E.; Zhang, H.; Yang, B.; Ren, H.; Shen, J., Preparation of luminescent polyelectrolyte/Cu-doped ZnSe nanoparticle multilayer composite films. *J. Colloid Interface Sci.* **2001,** 238, (2), 285-290.
54. Gul, S.; Cooper, J. K.; Corrado, C.; Vollbrecht, B.; Bridges, F.; Guo, J.; Zhang, J. Z., Synthesis, optical and structural properties, and charge carrier dynamics of Cu-doped ZnSe nanocrystals. *J. Phys. Chem. C* **2011,** 115, (43), 20864-20875.
55. Palve, B. M.; Jadkar, S. R.; Pathan, H. M., A simple chemical route to synthesize the umangite phase of copper selenide (Cu_3Se_2) thin film at room temperature. *J. Semicond.* **2017,** 38, (6), 063003.

56. Nelson, P. I.; Kannan, R. R.; Mohan, A.; Rajesh, S.; Vidhya, B., Impact of sequential annealing on the characteristics of thermally evaporated semiconductor $Cu_2Se/ZnSe/Cu_2Se$ sandwich structure. *J. Mater. Sci.: Mater. Electron.* **2018,** 29, (9), 7393-7401.
57. Pinto, A. H.; Leite, E. R.; Longo, E.; de Camargo, E. R., Crystallization at room temperature from amorphous to trigonal selenium as a byproduct of the synthesis of water dispersible zinc selenide. *Mater. Lett.* **2012,** 87, 62-65.
58. Nesheva, D.; Scepanovic, J. M.; Askrabic, S.; Levi, Z.; Bineva, I.; Popovic, Z., Raman scattering from ZnSe nanolayers. *Acta Phys. Pol.-Series A General Physics* **2009,** 116, (1), 75.
59. Shan, C.; Liu, Z.; Zhang, X.; Wong, C.; Hark, S., Wurtzite ZnSe nanowires: growth, photoluminescence, and single-wire Raman properties. *Nanotechnology* **2006,** 17, (22), 5561.
60. Milman, V., Klockmannite, CuSe: structure, properties and phase stability from ab initio modeling. *Acta Crystallogr. Section B: Structural Science* **2002,** 58, (3), 437-447.
61. Kaviyarasu, K.; Ayeshamariam, A.; Manikandan, E.; Kennedy, J.; Ladchumananandasivam, R.; Gomes, U. U.; Jayachandran, M.; Maaza, M., Solution processing of CuSe quantum dots: Photocatalytic activity under RhB for UV and visible-light solar irradiation. *Mater. Sci. Eng. B* **2016,** 210, 1-9.
62. Suyver, J.; Wuister, S.; Kelly, J.; Meijerink, A., Luminescence of nanocrystalline ZnSe: Mn^{2+}. *Phys. Chem. Chem. Phys.* **2000,** 2, (23), 5445-5448.
63. Gheshlaghi, N.; Pisheh, H. S.; Ünlü, H., Composition and strain effects in type i and type ii heterostructure ZnSe/Cd (Zn)S and $ZnSe/Cd_{1-x}Zn_xS$ core/shell quantum dots. *Superlattices Microst.* **2017,** 111, 156-165.
64. Philipose, U.; Saxena, A.; Ruda, H. E.; Simpson, P.; Wang, Y.; Kavanagh, K., Defect studies of ZnSe nanowires. *Nanotechnology* **2008,** 19, (21), 215715.
65. Manna, L.; Milliron, D. J.; Meisel, A.; Scher, E. C.; Alivisatos, A. P., Controlled growth of tetrapod-branched inorganic nanocrystals. *Nat. Mater.* **2003,** 2, (6), 382.
66. Fiore, A.; Mastria, R.; Lupo, M. G.; Lanzani, G.; Giannini, C.; Carlino, E.; Morello, G.; De Giorgi, M.; Li, Y.; Cingolani, R., Tetrapod-shaped colloidal nanocrystals of II− VI semiconductors prepared by seeded growth. *J. Am. Chem. Soc.* **2009,** 131, (6), 2274-2282.
67. Mews, A.; Kadavanich, A.; Banin, U.; Alivisatos, A., Structural and spectroscopic investigations of CdS/HgS/CdS quantum-dot quantum wells. *Phys. Rev. B* **1996,** 53, (20), R13242.
68. Sakr, G.; Yahia, I.; Fadel, M.; Fouad, S.; Romčević, N., Optical spectroscopy, optical conductivity, dielectric properties and new methods for determining the gap states of CuSe thin films. *J. Alloys Compd.* **2010,** 507, (2), 557-562.
69. Yeh, C.-Y.; Lu, Z.; Froyen, S.; Zunger, A., Zinc-blende–wurtzite polytypism in semiconductors. *Phys. Rev. B* **1992,** 46, (16), 10086.
70. Ito, T., Simple criterion for wurtzite-zinc-blende polytypism in semiconductors. *Jpn. J. Appl. Phys.* **1998,** 37, (10B), L1217.
71. Singh, S.; Liu, P.; Singh, A.; Coughlan, C.; Wang, J.; Lusi, M.; Ryan, K. M., Colloidal $Cu_2ZnSn(SSe)_4$ (CZTSSe) nanocrystals: shape and crystal phase control to form dots, arrows, ellipsoids, and rods. *Chem. Mater.* **2015,** 27, (13), 4742-4748.
72. Manna, L.; Scher, E. C.; Alivisatos, A. P., Synthesis of soluble and processable rod-, arrow-, teardrop-, and tetrapod-shaped CdSe nanocrystals. *J. Am. Chem. Soc.* **2000,** 122, (51), 12700-12706.
73. Kan, S.; Mokari, T.; Rothenberg, E.; Banin, U., Synthesis and size-dependent properties of zinc-blende semiconductor quantum rods. *Nat. Mater.* **2003,** 2, (3), 155.
74. Deng, Z.; Cao, L.; Tang, F.; Zou, B., A new route to zinc-blende CdSe nanocrystals: mechanism and synthesis. *J. Phys. Chem. B* **2005,** 109, (35), 16671-16675.
75. Mohamed, M. B.; Tonti, D.; Al-Salman, A.; Chemseddine, A.; Chergui, M., Synthesis of high quality zinc blende CdSe nanocrystals. *J. Phys. Chem. B* **2005,** 109, (21), 10533-10537.
76. Peng, Z. A.; Peng, X., Mechanisms of the shape evolution of CdSe nanocrystals. *J. Am. Chem. Soc.* **2001,** 123, (7), 1389-1395.
77. Murray, C.; Norris, D. J.; Bawendi, M. G., Synthesis and characterization of nearly monodisperse CdE (E= sulfur, selenium, tellurium) semiconductor nanocrystallites. *J. Am. Chem. Soc.* **1993,** 115, (19), 8706-8715.
78. Talapin, D. V.; Rogach, A. L.; Kornowski, A.; Haase, M.; Weller, H., Highly luminescent monodisperse CdSe and CdSe/ZnS nanocrystals synthesized in a hexadecylamine− trioctylphosphine oxide− trioctylphospine mixture. *Nano Lett.* **2001,** 1, (4), 207-211.
79. Mekis, I.; Talapin, D. V.; Kornowski, A.; Haase, M.; Weller, H., One-pot synthesis of highly luminescent CdSe/CdS core− shell nanocrystals via organometallic and "Greener" chemical approaches. *J. Phys. Chem. B* **2003,** 107, (30), 7454-7462.

80. Owen, J., The coordination chemistry of nanocrystal surfaces. *Science* **2015,** 347, (6222), 615-616.
81. Zeng, B.; Palui, G.; Zhang, C.; Zhan, N.; Wang, W.; Ji, X.; Chen, B.; Mattoussi, H., Characterization of the ligand capping of hydrophobic CdSe–ZnS quantum dots using NMR spectroscopy. *Chem. Mater.* **2017,** 30, (1), 225-238.
82. Turo, M. J.; Shen, X.; Brandon, N. K.; Castillo, S.; Fall, A. M.; Pantelides, S. T.; Macdonald, J. E., Dual-mode crystal-bound and X-type passivation of quantum dots. *Chem. Comm.* **2016,** 52, (82), 12214-12217.
83. Tao, A. R.; Habas, S.; Yang, P., Shape control of colloidal metal nanocrystals. *Small* **2008,** 4, (3), 310-325.

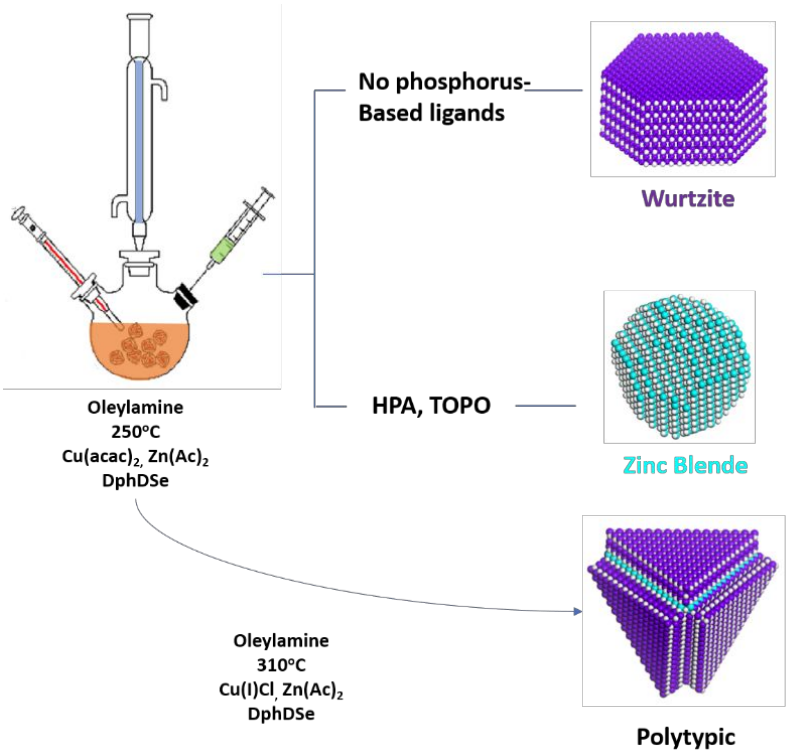
No phosphorus-
Based ligands
Wurtzite
HPA, TOPO
Zinc Blende
Oleylamine
250°C
Cu(acac)2, Zn(Ac)2
DphDSe
Oleylamine
310°C
Cu(I)Cl, Zn(Ac)2
DphDSe
Polytypic